

Electro-Optical Detection of Coherent Radiation Induced by Relativistic Electron Bunches in the Near and Far Fields

A. Curcio,^{1,2} M. Anania,¹ F. Bisesto,¹ M. Botton,³ M. Castellano,¹ E. Chiadroni,¹ A. Cianchi,⁴ M. Ferrario,¹ M. Galletti,¹ D. Giulietti,⁵ Z. Henis,³ M. Petrarca,⁶ R. Pompili,¹ E. Schleifer,³ and A. Zigler^{1,3}

¹*INFN-LNF, via Enrico Fermi 40, 00044 Frascati, Rome, Italy*

²*Department of Physics, “Sapienza” University of Rome, Piazzale A. Moro 2, I-00185 Rome, Italy*

³*Racah Institute of Physics, Hebrew University, Jerusalem 91904, Israel*

⁴*INFN and Department of Physics, “Tor Vergata” University, via della ricerca Scientifica 1, 00133 Rome, Italy*

⁵*Physics Department of the University and INFN, Largo Bruno Pontecorvo 3, 56127 Pisa, Italy*

⁶*Department of Basic and Applied Sciences for Engineering (SBAI) and INFN-Roma1, “Sapienza” University of Rome, Via A. Scarpa 14, 00161 Rome, Italy*

 (Received 28 July 2017; revised manuscript received 17 October 2017; published 6 February 2018)

Coherent radiation produced by relativistic charged bunches is nowadays of great interest for user-oriented applications and high-resolution diagnostics. Here we present experimental results obtained by using a temporal monitor based on the electro-optical sampling that allows us to reveal the features of the radiation emitted in terahertz range by ultrashort electron bunches moving in proximity to a nonlinear crystal. We investigate the radiation properties both in near- and far-field conditions by employing electron beams accelerated by a conventional photoinjector and through laser-plasma interactions. Our results indicate that the emitted radiation moves collinearly with the beam in one case, while its properties resemble those of the classical Cherenkov radiation in a second case.

DOI: [10.1103/PhysRevApplied.9.024004](https://doi.org/10.1103/PhysRevApplied.9.024004)

I. INTRODUCTION

In recent years, there has been growing interest in coherent radiation from electron bunches with femtosecond duration as intense sources of ultrashort light pulses. Electromagnetic radiation emitted in the millimeter and submillimeter (i.e., terahertz) range, in particular, is commonly used in many experiments to explore the microscopic structure of matter [1,2] and straightforward exploited as a high-resolution monitor to infer the inner properties (both longitudinal and transverse shape) of the bunches that generated it [3–6]. The main formation mechanisms, namely, synchrotron [7,8], transition [9,10], diffraction [11–13], Smith-Purcell [14–16], and Vavilov-Cherenkov [17,18], have been widely investigated so far. It is well known that all such kinds of processes arise from the field that is radiated when a charged particle undergoes acceleration [19], i.e., a variation of its velocity (in direction and/or modulo) due to an external field or to the crossing of the boundary between two different media [20]. Using such a formalism, it has been demonstrated that the emitted radiation patterns can be explained by describing particle motion via a series of discrete instantaneous acceleration events [21,22]. A common procedure adopted in many theoretical descriptions of the electromagnetic radiation consists of putting the observer (that is, the detector of the radiation) in the far-field region. Indeed, the near-field term

included in the Lienard-Wiechert potential (described in the following) becomes important, in general, when a large part of the charge distribution passes very close to the detectors, even if for most experiments, it represents only a minor correction at most. Here, we present an experimental investigation of the radiation that is induced in a dielectric medium by relativistic electron bunches with subpicosecond duration. The experiment is carried out at the SPARC_LAB test facility [23] by employing ultrashort electron bunches produced either by the high-brightness SPARC photoinjector [24,25] or through laser-plasma acceleration produced by the interaction of the 100-TW FLAME laser system [26] with solid targets [27,28]. We analyze, in particular, the radiation features both in the far- and near-field limit. We observe that in the first case, the typical propagation angle of the Vavilov-Cherenkov radiation (VCR) is obtained, while in the second one, the pattern of the VCR can be dominated by near-field effects, leading to a radiation front propagating in the same direction of the electron bunch that produces it. For this purpose, we develop a temporal diagnostics based on electro-optical sampling (EOS) [29,30], a nondestructive single-shot device frequently adopted in the accelerator community [31,32] due to its capability to provide a temporal resolution of the order of a few tens of femtoseconds [33]. The paper is organized as follows. The theoretical background together with a comprehensive description of the main goals is reported in

Sec. II. Section III describes the SPARC_LAB test facility and the main parameters of the electron bunches used for the experiment. Section IV describes the experimental setup of the EOS diagnostics developed for the SPARC photo-injector and the FLAME laser system. Finally, in Sec. V, we show the experimental results compared and validated by numerical simulations.

II. THEORETICAL BACKGROUND

The problem of radiation of electromagnetic waves by a single charged particle moving at an arbitrary velocity had correctly been formulated independently by Lienard and Wiechert before the advent of special relativity theory. According to their formulation, the radiation field is composed of two terms [19]. The first one called the *near-field* term falls as the square of the distance and reduces to the well-known Coulomb law for a particle at rest. The second one called the radiation term (*far field*) has the familiar scaling as the inverse of the distance and comes only from accelerated charges. In most practical applications, the first term presents only a minor correction to the observed fields since the observer is usually far from the field source where the radiation term dominates. On the contrary, if the detector is placed close to the source, the radiation term is overtaken by near-field effects.

A. Vavilov-Cherenkov radiation

It is well known that when a charged particle travels in a material medium (or close to it [34]) faster than the speed of light, Cherenkov radiation is emitted. Here, we are considering the radiation that moves in the medium, where the speed of light is renormalized to the medium refractive index. The basic mechanism is very similar to that of sound shock waves in gases [20]. For our purposes, we start from the Lienard-Wiechert potentials in the Fourier domain (\vec{k}, ω) , where \vec{k} is the total wave number and ω the angular frequency. For a particle moving at uniform speed $\vec{v} = v_0 \hat{z}$ along the \hat{z} direction, the retarded potentials are

$$\Phi(\vec{k}, \omega) = \frac{2\pi e}{\varepsilon(\omega)(k^2 - \frac{\omega^2}{c^2(\omega)})} \delta(\omega - \vec{k} \cdot \vec{v}), \quad (1)$$

$$\vec{A}(\vec{k}, \omega) = \frac{2\pi e \mu_0 \vec{v}}{(k^2 - \frac{\omega^2}{c^2(\omega)})} \delta(\omega - \vec{k} \cdot \vec{v}), \quad (2)$$

where $\varepsilon(\omega)$ and μ_0 are, respectively, the dielectric and magnetic permittivities, and $c(\omega) = 1/\sqrt{\varepsilon(\omega)\mu_0}$ is the speed of light in the medium. From the previous equations, the corresponding electric field is

$$\vec{E}(\vec{k}, \omega) = -i\vec{k}\Phi + i\omega\vec{A} = -\frac{2\pi i e}{\varepsilon(\omega)} \frac{\vec{k} - \frac{\omega\vec{v}}{c^2(\omega)}}{k^2 - \frac{\omega^2}{c^2(\omega)}} \delta(\omega - \vec{k} \cdot \vec{v}). \quad (3)$$

Its Fourier-Laplace inverse transforms give the distribution of the electromagnetic field in real space, namely,

$$\vec{E}(\vec{r}, \omega) = \frac{1}{(2\pi)^3} \int \vec{E}(\vec{k}, \omega) e^{i\vec{k} \cdot \vec{r}} d^3k, \quad (4)$$

where \vec{r} is the position vector. Because of the cylindrical symmetry involved in the problem, we can make use of the cylindrical coordinates (r, ϕ, z) and focus only on the z component of the electric field of Eq. (4) (the same applies to any other component). In formulas, we have

$$E_z(r, \omega) = i\omega \frac{e\mu_0}{2\pi} \left(1 - \frac{1}{\beta^2}\right) K_0(\alpha r) e^{i\{\omega z / \beta c(\omega)\}}, \quad (5)$$

where we introduce the modified Bessel function K_0 and the quantity

$$\alpha = -\frac{\omega}{c(\omega)} \sqrt{\frac{1}{\beta^2} - 1}, \quad (6)$$

with $\beta = \beta_0 c / c(\omega) = v_0 / c(\omega)$ the particle velocity normalized to the speed of light in the medium $c(\omega)$ (c is the speed of light in vacuum). In the far-field limit $|\alpha|r \gg 1$, from Eq. (5) it is $E_z \propto K_0(\alpha r) \propto \sqrt{\pi/2\alpha r} e^{-\alpha r}$, and for it to be propagating radially outward as a wave, α must be complex and, thus,

$$\beta > 1 \rightarrow v_0 > \frac{c}{\sqrt{\varepsilon(\omega)}}. \quad (7)$$

The Laplace transform of the axial electric field in Eq. (5), therefore, becomes proportional to $e^{i(k_r r + k_z z)}$, with $k_r = i\alpha = \omega \sqrt{1 - \beta^{-2}} / c(\omega)$ and $k_z = \omega / v_0$. By neglecting any absorption into the medium, we can write $\sqrt{\varepsilon(\omega)} \approx n$, with n the medium refractive index. In these conditions, the radiation propagates with an angle

$$\theta_c = \arcsin\left(\frac{k_z}{\sqrt{k_r^2 + k_z^2}}\right) = \arcsin\left(\frac{1}{\beta_0 n}\right), \quad (8)$$

which is the well-known expression of the Cherenkov angle whose formation mechanism is shown in Fig. 1. It is worth stressing that in order to observe Cherenkov radiation, we need for the condition of Eq. (7) to be satisfied and for the observer to be located *far* from the point source. If Eq. (7) is not fulfilled and/or there is no medium between the particle and the observer (i.e., we are in vacuum), no radiation is emitted since α will always be real, resulting in an evanescent wave.

B. Near- and far-field radiation

The expressions reported from Eqs. (1)–(6) are generally valid since no assumption has been done on the position of

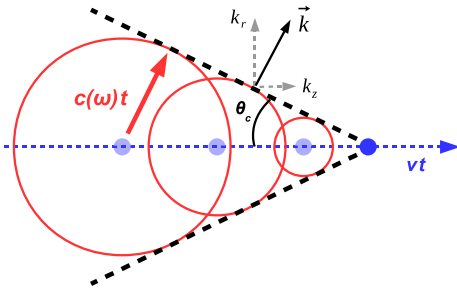


FIG. 1. Sketch of the Cherenkov radiation formation. The charged particle (blue circle) moves from left to right with velocity $v > c(\omega) = c/n(\omega)$. The overall wave front (black dashed lines) results from the coherent overlap of the radiation emitted along the particle path (red circles). It moves along the \vec{k} direction and is confined within a cone of aperture θ_c .

the observer. On the contrary, if the far-field condition holds, the well-known treatment of Cherenkov radiation comes out. The position of the observer with respect to the traveling particle is an important parameter that strongly affects the features of the emitted radiation. Nevertheless, it is usually neglected in many works because the detector of the radiation is assumed to be far from the particle path [17,22,35,36]. Proceeding by analogy with the previous section, we study the spatial Fourier transform of the E_z field in order to determine the radiation features (for instance, its propagation angle) when approaching the near-field conditions. The propagation of the electric field reported in Eq. (5) can be described by studying the radial Fourier transform of the function K_0 . Being k_z fixed by the particle velocity v_0 , the effective propagation angle of the radiation is determined by the specific value of k_r . By assuming now a generic spatial frequency k_r , we can define a new function

$$f(k_r) = \int K_0(\alpha r) e^{-ik_r r} dr = \frac{\pi}{2\sqrt{k_r^2 + \alpha^2}} \quad (9)$$

that is singular at $k_r = k_c = i\alpha$, i.e., in correspondence to the Cherenkov angle obtained in Eq. (8). Such a singularity can be removed by providing a more complete description of the medium that includes its absorption coefficient $\kappa(\omega)$. In such a way, the dielectric permittivity, therefore, becomes $\epsilon(\omega) = (n + i\kappa)^2$, and we can expand the α coefficient given in Eq. (6) as

$$\alpha \approx \frac{\omega}{c} (\kappa(\omega) - in(\omega)) \sqrt{1 - \frac{1}{n^2 \beta_0^2}}, \quad (10)$$

where small absorption of the field in the material is assumed. The propagation angle of the emitted radiation can, thus, be determined in terms of the probability

$$P(k_r) = \frac{|f(k_r)|^2}{\int_0^\infty dk_r |f(k_r)|^2} \quad (11)$$

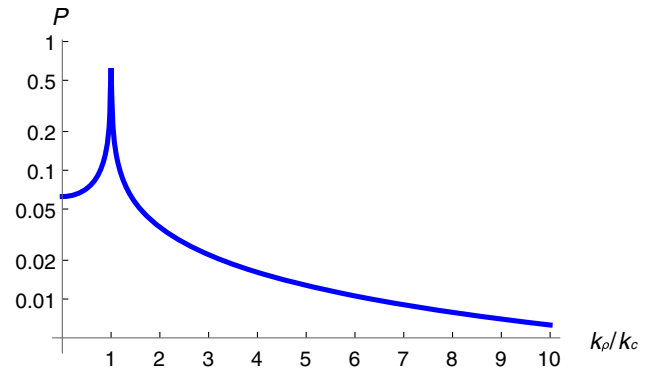


FIG. 2. Probability (reported in semilogarithmic scale) of finding a photon with radial momentum k_r . The maximum corresponds to $k_r/k_c = 1$, with $k_c = i\alpha$, i.e., the Cherenkov angle calculated in Eq. (8).

to find a photon with radial momentum $\hbar k_r$. Such a quantity as a function of the k_r/k_c ratio is shown in Fig. 2.

We should consider now that in our specific experimental conditions, the radiation is detected by means of a nonlinear crystal placed at a distance R from the moving bunch (cf., Sec. IV). As a consequence, its field is damped in vacuum by a factor $K_0(\alpha R) \propto e^{-\xi}$, where the quantity $\xi = 2\pi R/\gamma\beta_0\lambda$ (with $\gamma = 1/\sqrt{1-\beta_0^2}$ the relativistic Lorentz factor and $\lambda = 2\pi c_0/\omega$) actually determines the regime we are operating in. When $\xi \gg 1$, the far-field condition holds, while for $\xi \ll 1$, the near-field effects dominate. The effective spectrum of the spatial frequencies getting the crystal at point R can, therefore, be written as a product between the probability of Eq. (11) and the vacuum damping factor $K_0(\alpha R)$ (with the substitution $\lambda = 2\pi/k_r$). At zeroth order, we can simply set $k_{\min} = \gamma\beta_0/R$ corresponding to the assumption that all the wavelengths shorter than k_{\min} are exponentially damped out in vacuum and cannot reach the crystal. By considering the probability shown in Fig. 2 and that the average k_r at a distance R is given by

$$\bar{k}_r(R) = \int_{k_{\min}(R)}^\infty k_r P(k_r) dk_r, \quad (12)$$

one recognizes that $\bar{k}_r(R) \rightarrow k_c$ for $R \rightarrow \infty$, i.e., in the far-field condition $k_{\min} \rightarrow 0$. Such a picture corresponds to a radiation propagating at $90^\circ - \theta_c$, where θ_c is the Cherenkov angle of Eq. (8). For all the other cases, an effective propagation angle [reducing, in the far-field limit, to the angle complementary to that expressed by Eq. 8] can be defined. Starting from the average radial (\bar{p}_r) and longitudinal (\bar{p}_z) momenta of the electromagnetic field, the effective Cherenkov angle can be calculated as follows. The longitudinal momentum is given by $\bar{p}_z = N_z \hbar k_z = N_{\text{tot}} \hbar k_z$, where N_z is the number of photons and $\hbar k_z$ their average momentum. The Fourier transform of Eq. (5) in the domain of the longitudinal frequencies k_z is

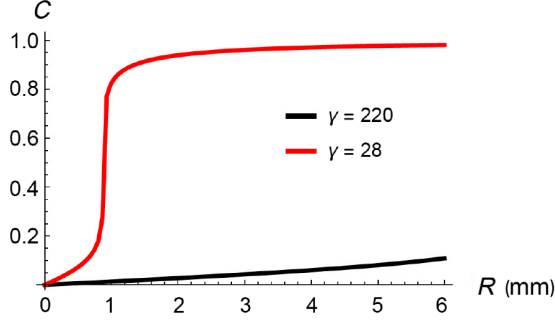


FIG. 3. Plot of the cumulative function of Eq. (13). Its interpretation is the probability of finding any photon with transverse momentum $\hbar k_r$ at the observation distance R . We consider a radiation wavelength $\lambda = 666 \mu\text{m}$ (0.45 THz).

$\delta(k_\zeta - k_z)$ because all the photons have the same longitudinal momentum $\bar{k}_z = k_z$. As a result, it is $N_z = N_{\text{tot}}$, with N_{tot} the total number of photons associated to the E_z field.

For the radial momentum, we get $\bar{p}_r = N_r \hbar \bar{k}_r$, where N_r is the number of photons with average momentum $\hbar \bar{k}_r$. The quantity N_r can be identically recast as $N_r = N_{\text{tot}} C(R)$, where $C(R)$ is the cumulative function of $P(k_r)$ defined as

$$C(R) = \int_{k_{\min}(R)}^{\infty} dk_r P(k_r). \quad (13)$$

The role of the $C(R)$ is to take into account how many photons with radial momentum $\hbar k_r$ reach the crystal. Figure 3 shows $C(R)$ as a function of the observer distance. The function is evaluated for two different bunch energies (corresponding to the experimental ones reported in Table I). One can see that in the far-field limit, $R \rightarrow \infty$ [or, equivalently, $k_{\min}(R) \rightarrow 0$, which is a low-energy bunch], $C \rightarrow 1$, and the average direction of the emitted radiation is the one determined by the Cherenkov angle ($k_r \rightarrow k_c$). In Fig. 3 (red line), it corresponds to the maximum probability to find the photons propagating at the Cherenkov angle because the photons tend to have transverse momentum $\hbar k_c$. On the contrary, in near-field conditions (higher-energy bunch), it is $C \ll 1$, and the average radial momentum is higher than $\hbar k_c$. The effective propagation angle, thus, becomes smaller than the angle complementary to that expressed by Eq. (8).

We can finally define the effective propagation angle of the emitted radiation as the complementary of

TABLE I. Typical bunch parameters obtained with the SPARC photoinjector and the FLAME laser facility.

Parameter	SPARC	FLAME
Charge	200 ± 10 pC	2.1 ± 0.2 nC
Energy	110.2 ± 0.3 MeV	14 ± 2 MeV
Duration	480 ± 35 fs	510 ± 25 fs

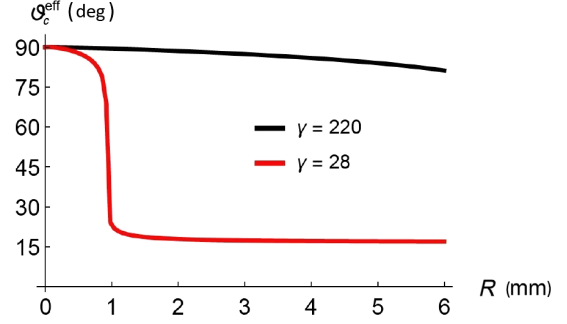


FIG. 4. The Cherenkov angle calculated through Eq. (14) versus the observation distance.

$$\begin{aligned} \theta_c^{\text{eff}}(R) &= \arcsin \left[\frac{\bar{p}_z}{\sqrt{\bar{p}_z^2 + \bar{p}_r^2}} \right] \\ &= \arcsin \left[\frac{k_z}{\sqrt{k_z^2 + [C(R)\bar{k}_r]^2}} \right] \end{aligned} \quad (14)$$

converging to the classical Cherenkov angle of Eq. (8) in the far-field limit. Figure 4 shows the effective Cherenkov angle as a function of the observation distance for the same two bunch energies. In the case $\gamma = 220$ and $R = 1$ mm, we get $\theta_c^{\text{eff}} \sim 88.8^\circ$, indicating a radiation front propagating almost parallel to the bunch propagation direction. On the contrary, for $\gamma = 28$ and $R = 1$ mm, we get $\theta_c^{\text{eff}} \sim 23.5^\circ$, close to the classical Cherenkov angle value $\theta_c = \arcsin(1/n\beta_0) \sim 18.2^\circ$.

All the quantities previously reported are calculated at the wavelength corresponding to the maximum of the radiation spectrum. Such a value is evaluated as follows. Starting from the Vavilov-Cherenkov energy spectrum (per unit length) of a single particle [19],

$$\left(\frac{d^2 I}{d\omega dz} \right)_{\text{SP}} = \frac{e^2}{4\pi\epsilon_0 c^2} \omega \left(1 - \frac{1}{\epsilon(\omega)\mu_0 v_0^2} \right), \quad (15)$$

and considering a bunch containing N_e electrons, the resulting radiation spectrum is

$$\left(\frac{d^2 I}{d\omega dz} \right)_{\text{tot}} = [N_e + N_e(N_e - 1)F(\omega)] \left(\frac{d^2 I}{d\omega dz} \right)_{\text{SP}}, \quad (16)$$

where $F(\omega) = \int S(\vec{r}') e^{i(\omega/c)\hat{r}\cdot\vec{r}'} d^3 r'$ is the bunch form factor, with $S(\vec{r}')$ the spatial distribution of the electron bunch and \hat{r} the unit vector pointing to the observer position. Since the EOS diagnostics we are employing is not sensitive to frequencies higher than approximately $\omega/2\pi \sim 5$ THz (cf., Sec. IV), we can neglect the incoherent term ($\propto N_e$) on the rhs of Eq. (16) and consider only its coherent part ($\propto N_e^2$). As shown in Fig. 5, for a Gaussian bunch with (rms) duration $\tau = 500$ fs (as the one we report in Table I), the peak on the radiation spectrum is obtained at

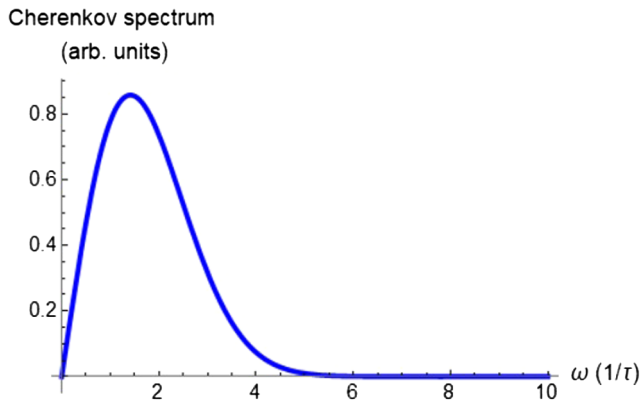


FIG. 5. Cherenkov radiation spectrum generated by a Gaussian electron bunch with (rms) duration $\tau = 500$ fs. The peak is positioned at $\omega = \sqrt{2}/\tau$, corresponding to a frequency $\nu = \omega/2\pi \sim 0.45$ THz.

$\omega/2\pi = 0.45$ THz. For such a frequency, the refractive and absorption indices of the zinc telluride (ZnTe) crystal are $n = 3.2$ and $\kappa = 2.9 \times 10^{-3}$, respectively.

III. SPARC_LAB TEST FACILITY

SPARC_LAB [23] (LNF-INFN) is a test facility based on the combination of high-brightness beams from the SPARC photoinjector [25] with high-power laser pulses produced by the FLAME laser [37]. The joint presence of these two systems allows the investigation of several plasma acceleration schemes, e.g., self- [38] and external injection [39], laser and beam driven [40], and a wide spectrum of interdisciplinary leading-edge research activities based on novel radiation sources such as free-electron laser both in self-amplified spontaneous emission (SASE), seeded, and exotic schemes [41,42], x-ray sources by means of Thomson scattering [43], high-power terahertz radiation, both broadband and narrow band [10,44], and able to fulfill user experiments [2]. To show the peculiarities of the radiation patterns in the near- and far-field limits, we employ both high- and low-energy electron bunches. These are obtained in the first case with the SPARC photoinjector producing 480-fs-long bunches with 200-pC charge and 110-MeV energy. On the other hand, low-energy (14 MeV) bunches with 500-fs duration and up to 2.1-nC charge are realized through laser-matter interactions by focusing the FLAME laser on metallic sharp targets, resulting in peak currents of the order of 2 kA [28]. These values are summarized in Table I.

A. High-brightness photoinjector

The SPARC photoinjector consists of an S-band 1.6-cell BNL-UCLA-SLAC-type rf gun providing 120-MV/m peak electric field on the built-in metallic (Cu) photocathode. The electrons extracted by means of UV laser pulses whose shape and duration can be tailored according to the

experimental task are accelerated up to 5.3 MeV in the gun [45] and then injected into the main linac acting as both a booster and longitudinal rf compressor by means of the velocity bunching technique [46,47]. Solenoid coils embedding the first two sections can provide additional magnetic focusing during VB process and control of emittance and envelope oscillations [48]. A diagnostics transfer line consisting of a spectrometer and a rf deflector allows for a complete 6D beam characterization (longitudinal phase space, projected, and slice emittance [49,50]). The machine tunability is very wide, so the final beam parameters are easily adjusted according to the task. Electron bunches 100 fs long with up to 600-pC charge have been produced so far [2,10]. At the opposite, ultrashort (approximately 30 fs) low-charge (approximately 20 pC) bunches as the ones required for laser- and beam-driven plasma acceleration schemes have also been realized [40,51].

B. FLAME laser system

The FLAME laser is based upon a Ti:Sa chirped-pulse amplification system delivering up to 5-J pulses with 30-fs (FWHM) duration at 800 nm (fundamental wavelength) and 10-Hz repetition rate. The resulting peak power is about 130 TW. The laser features a high-subnanosecond contrast ratio ($>10^{10}$) and can be focused on targets using an $f/10$ off-axis parabola resulting in a maximum intensity of the order of 10^{19} W/cm². Here, electron bunches with charge up to several nanocoulombs are produced through the interaction of the laser with metallic targets of different shapes [27]. The process is as follows. During the interaction, the target is ionized and free electrons are produced. A majority of them spread and dissipate energy inside of it, while the hot component of these electrons is able to reach the target's rear side and is released in vacuum [52]. Only the most energetic of these electrons can escape, leaving behind an electrostatic potential that locks the majority of them near the target. Such a potential set up by the unbalanced positive charge left on target [53] generates an electric field that can accelerate surface protons and ions in a process called target normal sheath acceleration [54].

IV. ELECTRO-OPTICAL SAMPLING DIAGNOSTICS

The EOS [29] is a single-shot nondestructive diagnostics that is able to provide temporal resolutions of the order of a few tens of femtoseconds [33] and widely used in accelerator facilities [30–32]. The EOS makes use of electro-optic crystals like ZnTe placed close to the electron-beam path. The large bunch Coulomb fields induce a local birefringence into the crystal that, as a consequence, becomes anisotropic. Such an anisotropy can be exploited to modulate the polarization of a probe laser pulse that simultaneously propagates into the crystal at velocity $v_L = c/n(\omega_L)$ (with ω_L the laser carrier frequency). By doing

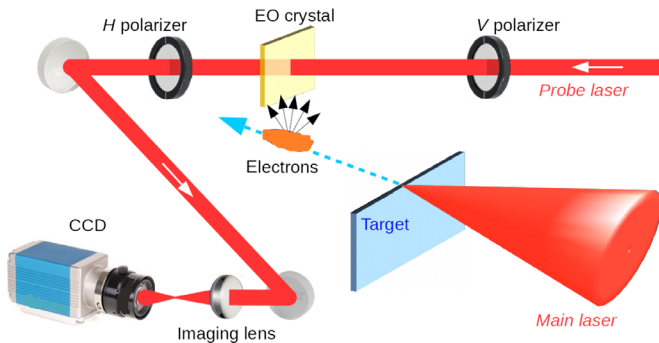


FIG. 6. Setup of the EOS diagnostics at FLAME. The electron beam is produced by the interaction of the FLAME laser with a metallic target. The ZnTe crystal located downstream from the target becomes birefringent during the passage of the electron beam and modulates the polarization of a probe laser crossing the crystal at the same time. By measuring the polarization modulation of the probe laser, the longitudinal beam profile is retrieved. The same EOS setup is also used for the SPARC photoinjector.

so, the bunch electric field is optically encoded into the laser pulse and can be experimentally retrieved. The final resolution of the EOS diagnostics is mainly dictated by the probe pulse duration and the electro-optic crystal employed. Considering the ZnTe, due to a phonon resonance located at 5.3 THz, the final resolution [assuming a probe laser with (rms) duration $\sigma_t \ll 100$ fs] is limited to approximately 100 fs [30]. It is well known that in order to work, the probe laser and the induced local birefringence must have approximately the same speed while moving into the crystal. For the local birefringence, it translates as a propagation speed $v_{\text{THz}} = c/n(\omega_{\text{THz}})$, where it is usually assumed that the transient electric field of the relativistic bunch moves along the crystal as a subpicosecond terahertz pulse [55]. In terms of temporal resolution, the best results are obtained when such a speed matches the laser velocity, i.e., $v_L \approx v_{\text{THz}}$. Since the local birefringence moves at v_{THz} , it means that it is actually induced by a *radiation field* and not directly by the moving bunch (that moves with speed c). We can, thus, conclude that the local birefringence is produced in the crystal by the radiation induced in turn by the relativistic bunch moving close to it. Therefore, the probe laser acts as a local observer (moving with proper velocity v_L), and, thus, the EOS diagnostics can be used in order to retrieve the properties of the radiation field.

At SPARC_LAB, two EOS-based devices have been developed so far. Both systems make use of a 500- μm -thick ZnTe crystal and employ the spatial encoding technique [31] in which the probe laser crosses the crystal with an angle of $\theta_i \approx 30^\circ$. In such a way, being x the spatial coordinate along the laser transverse profile and z the longitudinal coordinate along the electron bunch, z is encoded along x as $z = x \sin \theta_i$. The first system is currently installed on the SPARC photoinjector. It uses an IR probe laser ($\lambda = 800$ nm, 80-fs rms duration) directly split from the photocathode laser system, resulting in a natural synchronization with the electron

beam [56]. The second EOS device has been realized in the FLAME experimental area with the purpose of measuring the electron jets emitted after the interaction of the FLAME laser with a metallic solid target [27]. Similar to SPARC, here also the probe laser is directly split from the main laser ($\lambda = 800$ nm, 30-fs rms duration). In this specific case, we exploit the EOS as a time-of-arrival monitor in order to estimate the average energy of the emitted bunches [28]. The experimental setup is shown in Fig. 6.

V. EXPERIMENTAL RESULTS

In this section, we show the experimental results obtained with the EOS diagnostics from both SPARC and FLAME. In order to compare the results with the theoretical treatment discussed so far, we develop a numerical simulation code that reproduces the detection of electro-optic signals as the ones generated by the electron bunches reported in Table I. The code calculates the bunch electric field at distance R from the ZnTe crystal and takes into account its propagation along the crystal itself. Here, the propagating field induces a localized birefringence that is sampled by a simulated laser probe (a simulated replica of the experimental one). Finally, the code simulates the EOS response as detected by the CCD camera (see Fig. 6). More details about the simulation code are reported in Ref. [28]. The propagation direction of the field into the crystal (and, in turn, of the induced birefringence) is included as a free parameter. This choice allows us to simulate the EOS response at any angle and verify the conjectures described in Sec. II B.

A. Detection of electron bunches accelerated with the SPARC LINAC

We refer to a detection scheme similar to that of Fig. 6, changing only the source of electrons, which in this case is the SPARC LINAC, whose parameters are reported in Table I. During the experiment, the distance between the electron bunch and the ZnTe crystal is $R = 1$ mm. The mean electron energy is 110 MeV with an energy spread lower than a percent. The bunch duration is approximately 480 fs. With these parameters, the expectation concerning the propagation angle of the produced Cherenkov is well described by the theoretical curves in the previous section, in particular, Fig. 4. The effective propagation angle is $90^\circ - \theta_{\text{eff}} \sim 1.2^\circ$, indicating, when referring to Fig. 1, a radiation front propagating almost parallel to the direction of the electrons. In order to reproduce the signal registered on the CCD camera (Fig. 7), a radiation front propagating almost parallel to the electron bunch is considered, and the simulation perfectly agrees with the measurement (Fig. 7). Figure 7 reports the raw data resulting from the CCD camera. The axes are in pixel units. The entire image actually represents a snapshot of the EOS crystal surface, with the electro-optic signal coming out from it. The pixel can be calibrated in time (according to the EOS encoding),

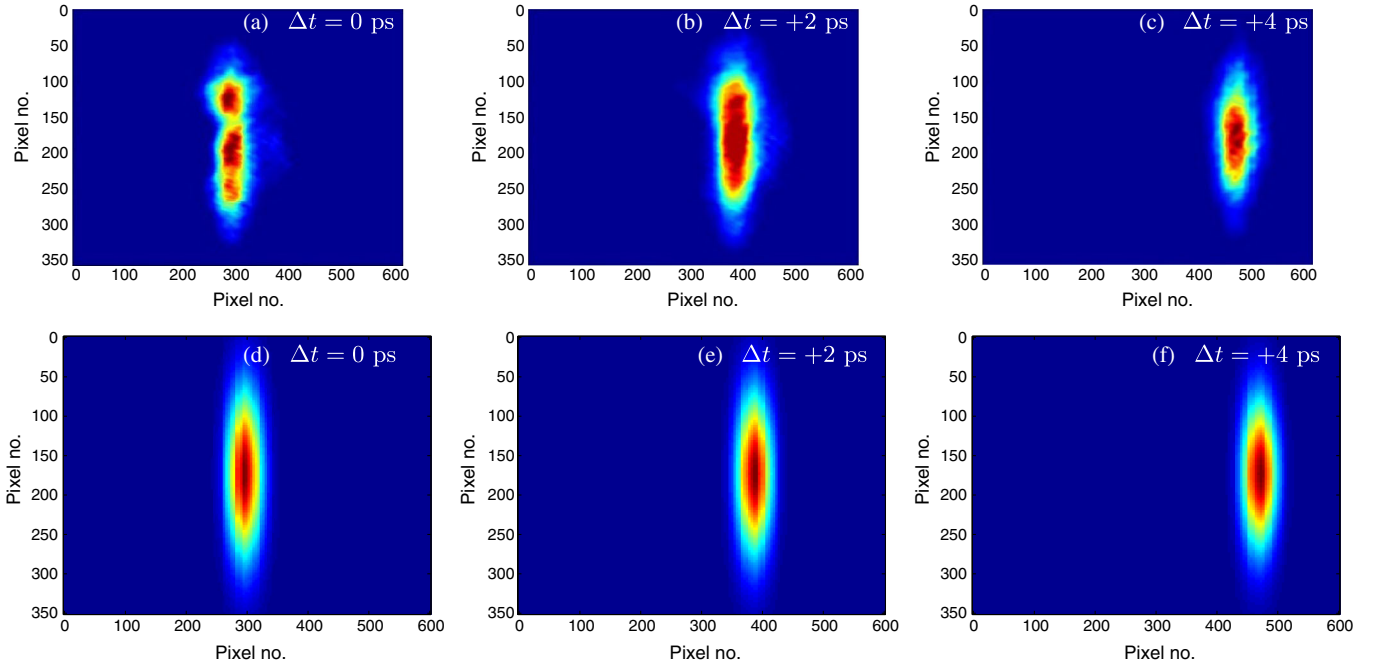


FIG. 7. (a)–(c) Experimentally measured EOS signals obtained by changing the probe laser delay (Δt) with respect to the time of arrival of the electron bunch. (d)–(f) Simulated EOS signals.

and the width of the signal represents the duration of the electron bunch that induces the electro-optic effect, as shown in Figs. 8 and 10 where the temporal axis is reported. The transverse size of the probe laser on the crystal is approximately 6 mm, corresponding to about a 10-ps time window. The lower and upper edges of the images are actually given by the CCD: the crystal is a (10 × 10)-mm surface, the CCD has an effective area of about 8 mm. We perform 1:1 imaging of the crystal onto the CCD; thus, only a portion of it is actually imaged on the CCD. The snapshots reported in Figs. 7(a)–7(c) (and then the same applies to Fig. 9) are all the same except for a different delay between them producing a horizontal shift of the signal, but its shape and features do not change at all. Therefore, the only information which could be extracted from the snapshots acquired at different delays is a time

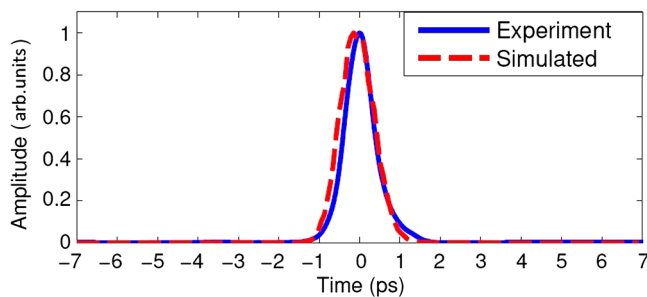


FIG. 8. By projecting the raw EOS signals along the horizontal axis, the bunch temporal profile is retrieved. The bunch parameters are the ones reported in Table I. The analysis refers to the signal of Figs. 7(a) and 7(d).

calibration of the x axis. Numerical simulations can correctly reproduce such a behavior. These simulations are reported in Figs. 7(d)–7(f) showing how the radiation field in the far-field regime sweeps by in time. Any other choice for the propagation angle of the nonlinear polarization inside the crystal, in particular, the choice of the Cherenkov angle [Eq. (8)] produces curved signals, while the measurements in Figs. 7 and 8 show a straight vertical line on the CCD screen. Therefore, we conclude that the theoretical considerations developed in the previous section are in good agreement with the data, and we can say that the crystal is in the near field of the electron bunch. In fact, Fig. 4 shows $\theta_c^{\text{eff}} \sim 90^\circ$ corresponding to the feature experimentally observed. This feature can be qualitatively understood just by observing that $\xi \ll 1$; in fact, $R \ll \gamma\beta_0\lambda/2\pi \sim 23$ cm (for $\lambda = 666$ μm). Furthermore, we investigate the opposite case, the far-field case, by accelerating electrons at lower energies via the interaction of the high-power laser FLAME with solid targets. This is presented in detail within the next subsection.

B. Detection of electron bunches accelerated with the FLAME laser

The experimental setup for the detection in this case is properly shown in Fig. 6. We are able to have high temporal resolution on the dynamics of the electrons ejected from the solid target. The fast electron part of the broad spectrum (extending from 0 to 14) is detected as a bunch with energy 14 ± 2 MeV, as we report in Table I. The distance R between the electrons and the ZnTe crystal is 1 mm also in this case. We see that for 14-MeV electrons at 1 mm, the effective

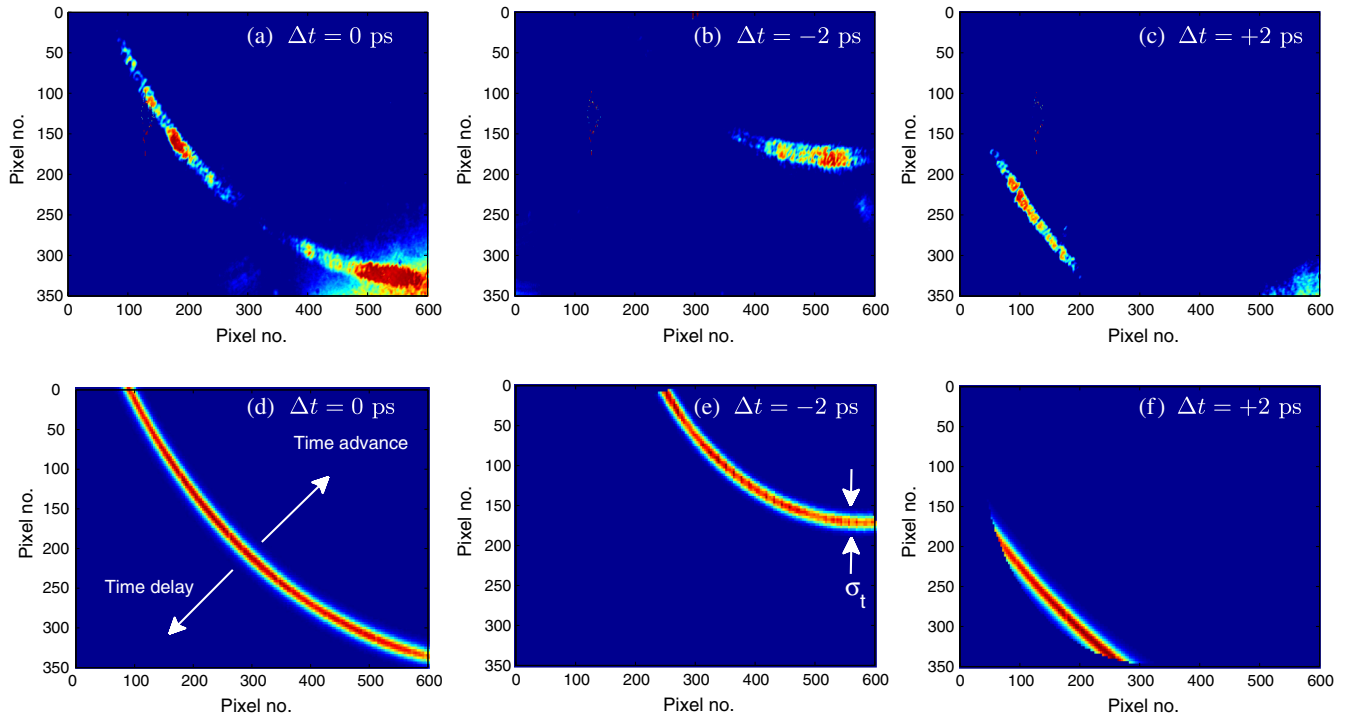


FIG. 9. (a)–(c) Experimentally measured EOS signals obtained by changing the probe laser delay (Δt) with respect to the main laser. The lack of uniformity in the experimental signals is mainly due to inhomogeneities both on the ZnTe crystal surface and on the transverse profile of the probe laser. (d)–(f) Simulated EOS signals. The time direction is indicated by the white arrows in (d). The lack of uniformity in the experimental signals is mainly due to inhomogeneities both on the ZnTe crystal surface and on the transverse profile of the probe laser.

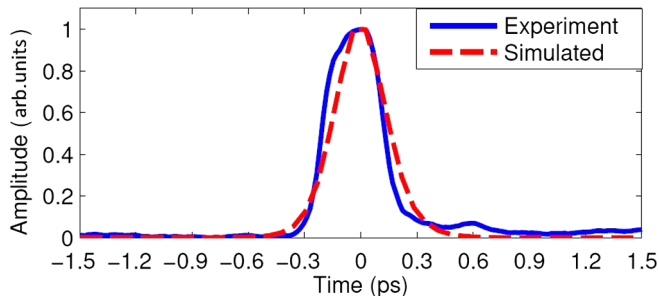


FIG. 10. The bunch temporal profile is proportional to the width of the detected signal. The bunch parameters are the ones reported in Table I. The analysis refers to the signal of Figs. 9(a) and 9(d).

propagation angle is already very close to $90^\circ - \theta_c = 71.8^\circ$. In order to reproduce the experimental data on the CCD (Fig. 9), we need to consider in the simulation code a propagation angle for the nonlinear polarization, which is approximately 67° , in agreement with Fig. 4. In Fig. 9, the measured EOS signals obtained by changing the probe laser delay (Δt) with respect to the main laser are reported. The curvature of the signals is due to a radiation front propagating inside the EOS crystal with an angle close to $90^\circ - \theta_c$, different than in Fig. 7 where straight signals are visible. The lack of uniformity in the experimental signals is mainly due

to inhomogeneities both on the ZnTe crystal surface and on the transverse profile of the probe laser. Furthermore, as shown in Fig. 9, the simulation results are in good agreement with the measurements, and we can reinforce the validity of the theory developed in the previous section, studying both the limits of the near and far field. In the case of laser-plasma accelerated electrons, we are in the far-field conditions ($\xi \gtrsim 1$); in fact, the condition $R \gtrsim \gamma\beta_0\lambda/2\pi$ (for $\lambda = 666 \mu\text{m}$) holds.

VI. CONCLUSIONS

The birefringence induced in nonlinear crystals by relativistic electron bunches traveling nearby is recognized to propagate as Vavilov-Cherenkov radiation through the medium. Part of the evanescent Coulomb field associated to the bunch traveling in vacuum can interact with the crystal medium. This is possible because the Coulomb field extension at the wavelength λ is approximately $\gamma\lambda/2\pi$. The interacting field induces a nonlinear polarization of the medium, which in the far field propagates as a wave at the angle complementary to the Cherenkov one. In the near field, the medium polarization resembles the Coulomb field of the bunch more than a radiation field, and it propagates straight. According to the electron energy and the distance between the electron bunch and the EOS diagnostics, the last can be considered in the near field or in the far field of the

Vavilov-Cherenkov radiation. Experiments are performed exploiting the SPARC LINAC and the FLAME laser of the INFN National Laboratories of Frascati. High-energy (110 MeV) electrons are provided by the SPARC LINAC, while low-energy (up to 14 MeV) electrons are accelerated during the interaction between the FLAME laser with a solid target. The only way to interpret the experimental data is to consider that in the case of LINAC-accelerated electrons, the EOS diagnostics is in the near field of the radiation induced inside the EOS crystal by the electron bunch, and it propagates straight on, in the same direction as the electrons. On the other hand, the laser-plasma accelerated electrons induce a nonlinear polarization wave propagating approximately complementary to the Cherenkov angle inside the EOS crystal; therefore, the detector should be considered in the far field.

ACKNOWLEDGMENTS

This work is partially supported by the EU Commission in the Seventh Framework Program, Grant No. 312453 EuCard-2 and by the Italian Ministry of Research in the framework of Fondo per gli Investimenti della Ricerca di Base, Project No. RBFR12NK5K.

-
- [1] Z. Wu, A. S. Fisher, J. Goodfellow, M. Fuchs, D. Daranciang, M. Hogan, H. Loos, and A. Lindenberg, Intense terahertz pulses from SLAC electron beams using coherent transition radiation, *Rev. Sci. Instrum.* **84**, 022701 (2013).
- [2] F. Giorgianni, E. Chiadroni, A. Rovere, M. Cestelli-Guidi, A. Perucchi, M. Bellaveglia, M. Castellano, D. Di Giovenale, G. Di Pirro, M. Ferrario, R. Pompili, C. Vaccarezza, F. Villa, A. Cianchi, A. Mostacci, M. Petrarca, M. Brahlek, N. Koirala, S. Oh, and S. Lupi, Strong nonlinear terahertz response induced by dirac surface states in Bi_2Se_3 topological insulator, *Nat. Commun.* **7**, 11421 (2016).
- [3] C. Behrens, F.J. Decker, Y. Ding, V.A. Dolgashev, J. Frisch, Z. Huang, P. Krejcik, H. Loos, A. Lutman, T.J. Maxwell, J. Turner, J. Wang, M.H. Wang, J. Welch, and J. Wu, Few femtosecond time-resolved measurements of x-ray free-electron lasers, *Nat. Commun.* **5**, 3762 (2014).
- [4] E. Chiadroni, M. Bellaveglia, P. Calvani, M. Castellano, L. Catani, A. Cianchi, G. Di Pirro, M. Ferrario, G. Gatti, O. Limaj, S. Lupi, B. Marchetti, A. Mostacci, E. Pace, L. Palumbo, C. Ronsivalle, R. Pompili, and C. Vaccarezza, Characterization of the THz radiation source at the Frascati linear accelerator, *Rev. Sci. Instrum.* **84**, 022703 (2013).
- [5] N.H. Matlis, G.R. Plateau, J. van Tilborg, and W.P. Leemans, Single-shot spatiotemporal measurements of ultrashort THz waveforms using temporal electric field cross correlation, *J. Opt. Soc. Am. B* **28**, 23 (2011).
- [6] S. Wesch, B. Schmidt, C. Behrens, H. Delsim-Hashemi, and P. Schmuser, A multi-channel THz and infrared spectrometer for femtosecond electron bunch diagnostics by single-shot spectroscopy of coherent radiation, *Nucl. Instrum. Methods Phys. Res., Sect. A* **665**, 40 (2011).
- [7] R. Jaspers, N.J. Lopes Cardozo, A. J. H. Donne, H. L. M. Widdershoven, and K. H. Finken, A synchrotron radiation diagnostics to observe relativistic runaway electrons in a tokamak plasma, *Rev. Sci. Instrum.* **72**, 466 (2001).
- [8] K. L. F. Bane, F. J. Decker, Y. Ding, D. Dowell, P. Emma, J. Frisch, Z. Huang, R. Iverson, C. Limborg-Deprey, H. Loos, H. D. Nuhn, D. Ratner, G. Stupakov, J. Turner, J. Welch, and J. Wu, Measurements and modeling of coherent synchrotron radiation and its impact on the linac coherent light source electron beam, *Phys. Rev. ST Accel. Beams* **12**, 030704 (2009).
- [9] E. Chiadroni *et al.*, "Characterization of the THz source at SPARC," in *Proceedings of IPAC 2010*, p. 627.
- [10] F. Giorgianni, M. P. Anania, M. Bellaveglia, A. Biagioni, E. Chiadroni, A. Cianchi, M. Daniele, M. Del Franco, D. Di Giovenale, G. Di Pirro, M. Ferrario, S. Lupi, A. Mostacci, M. Petrarca, S. Pioli, R. Pompili, V. Shpakov, C. Vaccarezza, and F. Villa, Tailoring of highly intense THz radiation through high brightness electron beams longitudinal manipulation, *Appl. Sci.* **6**, 56 (2016).
- [11] Y. Shibata, S. Hasebe, K. Ishi, T. Takahashi, T. Ohsaka, M. Ikezawa, T. Nakazato, M. Oyamada, S. Urasawa, T. Yamakawa, and Y. Kondo, Observation of coherent diffraction radiation from bunched electrons passing through a circular aperture in the millimeter- and submillimeter-wavelength regions, *Phys. Rev. E* **52**, 6787 (1995).
- [12] M. Castellano, V.A. Verzilov, L. Catani, A. Cianchi, G. Orlandi, and M. Geitz, Measurements of coherent diffraction radiation and its application for bunch length diagnostics in particle accelerators, *Phys. Rev. E* **63**, 056501 (2001).
- [13] A. Cianchi, M. Castellano, L. Catani, E. Chiadroni, K. Honkavaara, and G. Kube, Nonintercepting electron beam size monitor using optical diffraction radiation interference, *Phys. Rev. ST Accel. Beams* **14**, 102803 (2011).
- [14] G. Doucas, J.H. Mulvey, M. Otori, J. Walsh, and M.F. Kimmitt, First Observation of Smith-Purcell Radiation from Relativistic Electrons, *Phys. Rev. Lett.* **69**, 1761 (1992).
- [15] K. Ishi, Y. Shibata, T. Takahashi, S. Hasebe, M. Ikezawa, K. Takami, T. Matsuyama, K. Kobayashi, and Y. Fujita, Observation of coherent Smith-Purcell radiation from short-bunched electrons, *Phys. Rev. E* **51**, R5212 (1995).
- [16] S.E. Korbly, A.S. Kesar, J.R. Sirigiri, and R.J. Temkin, Observation of Frequency-Locked Coherent Terahertz Smith-Purcell Radiation, *Phys. Rev. Lett.* **94**, 054803 (2005).
- [17] T. Takahashi, Y. Shibata, K. Ishi, M. Ikezawa, M. Oyamada, and Y. Kondo, Observation of coherent Cherenkov radiation from a solid dielectric with short bunches of electrons, *Phys. Rev. E* **62**, 8606 (2000).
- [18] M. Shevelev, H. Deng, A. Potylitsyn, G. Naumenko, J. Zhang, Sh. Lu, S. Gogolev, and D. Shkitov, Sub-millimeter bunch length non-invasive diagnostics based on the diffraction and Cherenkov radiation, *J. Phys. Conf. Ser.* **357**, 012023 (2012).
- [19] J.D. Jackson, *Classical Electrodynamics* (John Wiley & Sons Inc., New York, 1999).
- [20] V.L. Ginzburg, Radiation by uniformly moving sources (Vavilov-Cherenkov effect, transition radiation, and other phenomena), *Phys. Usp.* **39**, 973 (1996).
- [21] I. E. T. I. M. Frank and I. G. Tamm, Coherent visible radiation from fast electrons passing through matter, *C. R. Acad. Sci. USSR* **14**, 109 (1937).

- [22] C. W. James, H. Falcke, T. Huege, and M. Ludwig, General description of electromagnetic radiation processes based on instantaneous charge acceleration in “endpoints,” *Phys. Rev. E* **84**, 056602 (2011).
- [23] M. Ferrario *et al.*, SPARC lab present and future, *Nucl. Instrum. Methods Phys. Res., Sect. B* **309**, 183 (2013).
- [24] M. Ferrario *et al.*, Direct Measurement of the Double Emittance Minimum in the Beam Dynamics of the SPARC High-Brightness Photoinjector, *Phys. Rev. Lett.* **99**, 234801 (2007).
- [25] D. Alesini *et al.*, The SPARC project: A high-brightness electron beam source at LNF to drive a SASE-FEL experiment, *Nucl. Instrum. Methods Phys. Res., Sect. A* **507**, 345 (2003).
- [26] F. G. Bisesto, M. P. Anania, E. Chiadroni, A. Cianchi, G. Costa, A. Curcio, M. Ferrario, M. Galletti, R. Pompili, E. Schleifer, and A. Zigler, Innovative single-shot diagnostics for electrons accelerated through laser-plasma interaction at FLAME, *Proc. SPIE Int. Soc. Opt. Eng.* **10240**, 102400K (2017).
- [27] R. Pompili, M. P. Anania, F. Bisesto, M. Botton, M. Castellano, E. Chiadroni, A. Cianchi, A. Curcio, M. Ferrario, M. Galletti, Z. Heniz, M. Petrarca, E. Schleifer, and A. Zigler, Femtosecond dynamics of energetic electrons in high intensity laser-matter interactions, *Sci. Rep.* **6**, 35000 (2016).
- [28] R. Pompili, M. P. Anania, F. Bisesto, M. Botton, M. Castellano, E. Chiadroni, A. Cianchi, A. Curcio, M. Ferrario, M. Galletti, Z. Henis, M. Petrarca, E. Schleifer, and A. Zigler, Sub-picosecond snapshots of fast electrons from high intensity laser-matter interactions, *Opt. Express* **24**, 29512 (2016).
- [29] I. Wilke, A. M. MacLeod, W. A. Gillespie, G. Berden, G. M. H. Knippels, and A. F. G. Van Der Meer, Single-Shot Electron-Beam Bunch Length Measurements, *Phys. Rev. Lett.* **88**, 124801 (2002).
- [30] B. Steffen, V. Arsov, G. Berden, W. A. Gillespie, S. P. Jamison, A. M. MacLeod, A. F. G. van der Meer, P. J. Phillips, H. Schlarb, B. Schmidt, and P. Schmuser, Electro-optic time profile monitors for femtosecond electron bunches at the soft x-ray free-electron laser flash, *Phys. Rev. ST Accel. Beams* **776**, 032802 (2009).
- [31] A. L. Cavalieri *et al.*, Clocking Femtosecond X Rays, *Phys. Rev. Lett.* **94**, 114801 (2005).
- [32] R. Pompili *et al.*, Femtosecond timing-jitter between photocathode laser and ultra-short electron bunches by means of hybrid compression, *New J. Phys.* **18**, 083033 (2016).
- [33] M. H. Helle, D. F. Gordon, D. Kaganovich, and A. Ting, Extending electro-optic detection to ultrashort electron beams, *Phys. Rev. ST Accel. Beams* **15**, 052801 (2012).
- [34] D. De Zutter and D. De Vleeschauwer, Radiation from and force acting on a point charge moving through a cylindrical hole in a conducting medium, *J. Appl. Phys.* **59**, 4146 (1986).
- [35] T. Takahashi, T. Kanai, Y. Shibata, K. Ishi, M. Ikezawa, T. Nakazato, M. Oyamada, S. Urasawa, T. Yamakawa, K. Takami, T. Matsuyama, K. Kobayashi, and Y. Fujita, Cherenkov radiation from a finite trajectory of electrons, *Phys. Rev. E* **50**, 4041 (1994).
- [36] J. Zheng, C. X. Yu, Z. J. Zheng, and K. A. Tanaka, Cherenkov radiation generated by a beam of electrons revisited, *Phys. Plasmas* **12**, 093105 (2005).
- [37] A. Curcio, M. P. Anania, F. Bisesto, E. Chiadroni, A. Cianchi, M. Ferrario, F. Filippi, D. Giulietti, A. Marocchino, F. Mira, M. Petrarca, V. Shpakov, and A. Zigler, Single-shot non-intercepting profile monitor of plasma-accelerated electron beams with nanometric resolution, *Appl. Phys. Lett.* **111**, 133105 (2017).
- [38] A. Curcio, M. P. Anania, F. Bisesto, E. Chiadroni, A. Cianchi, M. Ferrario, F. Filippi, D. Giulietti, A. Marocchino, M. Petrarca, V. Shpakov, and A. Zigler, Trace-space reconstruction of low-emittance electron beams through betatron radiation in laser-plasma accelerators, *Phys. Rev. ST Accel. Beams* **20**, 012801 (2017).
- [39] A. R. Rossi, A. Bacci, M. Belleveglia, E. Chiadroni, A. Cianchi, G. Di Pirro, M. Ferrario, A. Gallo, G. Gatti, C. Maroli, A. Mostacci, Vittoria Petrillo, Luca Serafini, Paolo Tomassini, and C. Vaccarezza, The external-injection experiment at the SPARC_LAB facility, *Nucl. Instrum. Methods Phys. Res., Sect. A* **740**, 60 (2014).
- [40] S. Romeo, M. P. Anania, E. Chiadroni, M. Croia, M. Ferrario, A. Marocchino, R. Pompili, and C. Vaccarezza, Beam dynamics in resonant plasma Wakefield acceleration at SPARC_LAB, *Nucl. Instrum. Methods Phys. Res., Sect. A* **829**, 109 (2016).
- [41] V. Petrillo *et al.*, Observation of Time-Domain Modulation of Free-Electron-Laser Pulses by Multi-peaked Electron-Energy Spectrum, *Phys. Rev. Lett.* **111**, 114802 (2013).
- [42] L. Giannessi *et al.*, Self-Amplified Spontaneous Emission Free-Electron Laser with an Energy-Chirped Electron Beam and Undulator Tapering, *Phys. Rev. Lett.* **106**, 144801 (2011).
- [43] C. Vaccarezza *et al.*, The SPARC_LAB Thomson source, *Nucl. Instrum. Methods Phys. Res., Sect. A* **829**, 237 (2016).
- [44] E. Chiadroni *et al.*, The SPARC linear accelerator based terahertz source, *Appl. Phys. Lett.* **102**, 094101 (2013).
- [45] A. Cianchi *et al.*, High brightness electron beam emittance evolution measurements in an rf photoinjector, *Phys. Rev. ST Accel. Beams* **11**, 032801 (2008).
- [46] L. Serafini, M. Ferrario, C. Pellegrini, M. Cornacchia, S. Chattopadhyay, and I. Lindau, Velocity bunching in photoinjectors, *AIP Conf. Proc.* **581**, 87 (2001).
- [47] R. Pompili *et al.*, Beam manipulation with velocity bunching for PWFA applications, *Nucl. Instrum. Methods Phys. Res., Sect. A* **829**, 17 (2016).
- [48] M. Ferrario *et al.*, Experimental Demonstration of Emittance Compensation with Velocity Bunching, *Phys. Rev. Lett.* **104**, 054801 (2010).
- [49] D. Filippetto *et al.*, Phase space analysis of velocity bunched beams, *Phys. Rev. ST Accel. Beams* **952**, 092804 (2011).
- [50] A. Cianchi, D. Alesini, M. P. Anania, A. Bacci, M. Bellaveglia, M. Castellano, E. Chiadroni, D. Di Giovenale, G. P. Di Pirro, M. Ferrario, A. Gallo, L. Innocenti, A. Mostacci, R. Pompili, A. R. Rossi, J. Scifo, V. Shpakov, C. Vaccarezza, and F. Villa, Six-dimensional measurements of trains of high brightness electron bunches, *Phys. Rev. ST Accel. Beams* **18**, 082804 (2015).
- [51] A. R. Rossi *et al.*, Stability study for matching in laser driven plasma acceleration, *Nucl. Instrum. Methods Phys. Res., Sect. A* **829**, 67 (2016).

- [52] J. L. Dubois, F. Lubrano-Lavaderci, D. Raffestin, J. Ribolzi, J. Gazave, A. Compant La Fontaine, E. d'Humieres, S. Hulin, Ph. Nicolai, and A. Poye, Target charging in short-pulse-laser-plasma experiments, *Phys. Rev. E* **89**, 013102 (2014).
- [53] A. Poye, J. L. Dubois, F. Lubrano-Lavaderci, E. d'Humieres, M. Bardon, S. Hulin, M. Bailly-Grandvaux, J. Ribolzi, D. Raffestin, and J. J. Santos, Dynamic model of target charging by short laser pulse interactions, *Phys. Rev. E* **92**, 043107 (2015).
- [54] S. C. Wilks, A. B. Langdon, T. E. Cowan, M. Roth, M. Singh, S. Hatchett, M. H. Key, D. Pennington, A. MacKinnon, and R. A. Snavely, Energetic proton generation in ultra-intense laser-solid interactions, *Phys. Plasmas* **8**, 542 (2001).
- [55] S. Casalbuoni, H. Schlarb, B. Schmidt, P. Schmuser, B. Steffen, and A. Winter, Numerical studies on the electro-optic detection of femtosecond electron bunches, *Phys. Rev. ST Accel. Beams* **11**, 072802 (2008).
- [56] R. Pompili, A. Cianchi, D. Alesini, M. P. Anania, A. Bacci, M. Bellaveglia, M. Castellano, E. Chiadroni, D. Di Giovenale, G. Di Pirro, G. Gatti, F. Giorgianni, M. Ferrario, S. Lupi, F. Massimo, A. Mostacci, A. R. Rossi, C. Vaccarezza, and F. Villa, First single-shot and non-intercepting longitudinal bunch diagnostics for comb-like beam by means of electro-optic sampling, *Nucl. Instrum. Methods Phys. Res., Sect. A* **216**, 740 (2014).